J Nanopart Res (2026) 28:100
https://doi.org/10.1007/s11051-026-06623-z

RESEARCH

Sonocatalytic and photocatalytic antibiotic removal using g-C_3N_4/carbon black

Hafize Nagehan Koysuren · Sumyah Amer Yahya · Ozcan Koysuren

Received: 2 February 2026 / Accepted: 18 March 2026 / Published online: 31 March 2026

Abstract This study presented a simple heat treatment process to synthesize graphitic carbon nitride (g-C_3N_4)/carbon black (CB) composites for applications in photocatalytic and sonocatalytic antibiotic degradation. The chemical and crystal structure, morphology, surface chemical composition and surface structure, and optical properties of g-C_3N_4/CB composites were studied using FTIR, XRD, FESEM, XPS, N_2 adsorption/desorption analyses, and UV–Vis absorption spectroscopy. The antibiotic degradation ability of g-C_3N_4/CB composites was evaluated separately under visible light irradiation and ultrasonic irradiation. The degradation experiments revealed that both the photocatalytic and sonocatalytic performance were affected by the carbon black concentration of the samples. Although no significant change was observed in the adsorption capacity of g-C_3N_4/CB, the photocatalytic and sonocatalytic performance of g-C_3N_4/CB showed a significant improvement compared to pure g-C_3N_4. The best photocatalytic and sonocatalytic performance was obtained with the composite containing 1 wt% of carbon black. The specified composite sample could remove 54.7% of tetracycline after 120 min of visible light irradiation and 53.4% of tetracycline after 120 min of ultrasonic irradiation. Radical trapping experiments revealed that superoxide radicals played a major role in the photocatalytic tetracycline degradation. Both superoxide and hydroxyl radicals played important roles in the sonocatalytic removal of tetracycline. g-C_3N_4/CB composites demonstrated reusability for tetracycline degradation over five consecutive cycles, maintaining a removal efficiency of 43.9% and 43.0% by photocatalytic and sonocatalytic process, respectively.

Supplementary Information The online version contains supplementary material available at https://doi.org/10.1007/s11051-026-06623-z.

H. N. Koysuren
Department of Environmental Engineering, Kirsehir Ahi Evran University, Kirsehir 40100, Turkey

S. A. Yahya · O. Koysuren (✉)
Department of Energy Systems Engineering, Ankara University, Ankara 06830, Turkey
e-mail: koysuren@ankara.edu.tr

Graphical Abstract

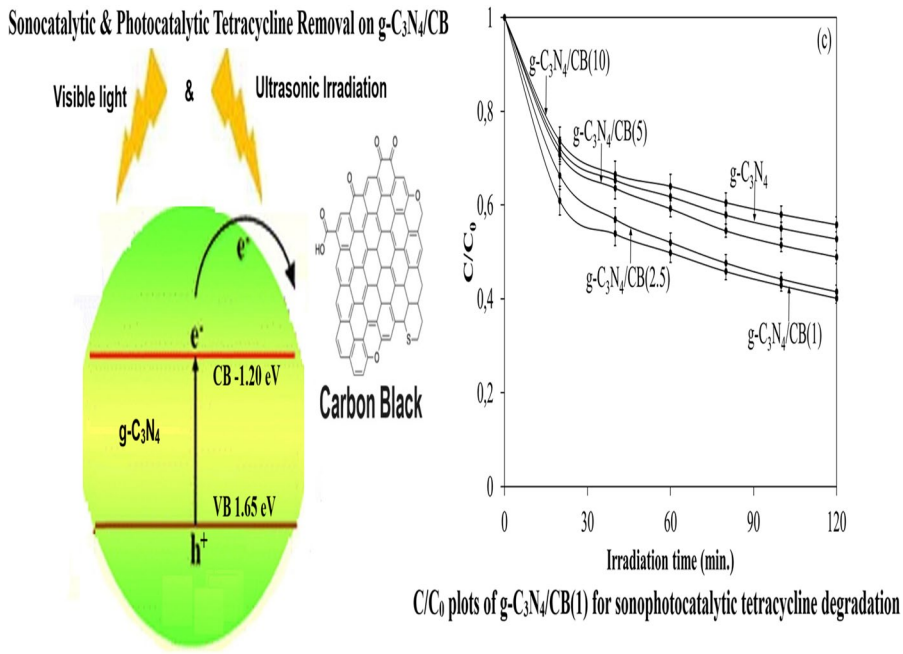

Keywords Photocatalytic activity · Sonocatalytic activity · g-C_3N_4 · Carbon black · Tetracycline

Introduction

Today, there is an increase in the discharge of complex wastewater streams containing heavy metals, organic pollutants, and various pharmaceuticals. Antibiotics constitute a significant fraction of the pharmaceuticals in the wastewater streams [1]. Antibiotics, exhibiting antimicrobial activities, are pharmaceuticals obtained from organic sources such as microorganisms, plants, and animals [2]. Antibiotics have been used to treat bacterial diseases in animals and humans or to promote growth in animals [2]. Among the antibiotics, tetracycline, as a class of broad-spectrum antibacterial agents with low cost and high antimicrobial activity, represents the second-largest class of antibiotics in the world [3]. However, tetracycline could not be completely utilized by organisms. Only 25% to 33% of the tetracycline could be absorbed by the human body and the animal body. The rest is released into the environment through feces and urine [2, 3]. Consequently, tetracycline tends to accumulate in the environment, particularly in soil and water systems [4]. The presence of tetracycline or other types of antibiotics poses a serious threat to both ecological safety and public health [4]. They lead to the formation of antibiotic-resistant genes and antibiotic-resistant bacteria [3]. Meanwhile, the risk is considered to be long-term due to the persistent effects of tetracycline and similar antibiotics. Due to its stable chemical structure, tetracycline does not completely decompose in the environment [4]. Therefore, it is important that tetracycline is effectively removed from the environment by converting it into non-toxic byproducts.

To date, researchers have focused intensely on developing a cost-effective, highly efficient, environmentally friendly, and simple treatment technique for removing antibiotics from the wastewater [2]. Photocatalysis technology has been widely used to degrade antibiotics and other organic pollutants in aquatic environments due to its simple working principle, efficiency, and environmentally friendly nature [3]. The photocatalysis technology harnesses light to activate photocatalysts, leading to the formation of photoexcited electron–hole pairs on the photocatalyst. The photoexcited charge carriers lead to the generation of reactive species such as superoxide and hydroxyl

radicals, enabling the efficient degradation of organic pollutants into non-toxic compounds [1]. As an alternative to photocatalysis, sonocatalysis has also been accepted as a suitable technique for removing tetracycline and similar antibiotics from aquatic environments. In recent years, sonocatalysis, as another advanced oxidation process, has attracted considerable attention because of its high efficiency, low investment cost, and simple process conditions [5, 6]. The sonocatalysis technique is based on ultrasonic irradiations, leading to the formation of acoustic cavitation in the liquid medium. The acoustic cavitation process involves the formation, growth, and collapse of cavitation bubbles in the liquid medium. The collapse of these cavitation bubbles leads to high temperature and pressure points, known as hot spots, in liquids, triggering the formation of hydroxyl and hydrogen radicals [6]. The hydrogen radicals can react with dissolved oxygen molecules to form superoxide radicals. All of these radicals can effectively degrade tetracycline and other organic pollutants in the liquid medium [5]. In addition, the collapse of the cavitation bubbles causes the emission of sonoluminescence with a wide wavelength of lights. Some catalysts can be activated by the sonoluminescence, which leads to the formation of sonoexcited electron–hole pairs on the catalyst, similar to photoexcited charge carriers. Sonoexcited electrons and holes can react with dissolved oxygen and water molecules to form superoxide and hydroxyl radicals, respectively; these radicals can directly decompose tetracycline and other organic pollutants [5, 6]. To date, a wide variety of catalysts have been investigated for use in photocatalytic and sonocatalytic reactions for the removal of tetracycline and other antibiotics.

Among catalysts, graphitic carbon nitride (g-C_3N_4) holds an important place as a highly efficient photocatalyst/sonocatalyst that can operate under both visible light and ultrasonic wave irradiations [7]. g-C_3N_4 has attracted great attention as a photocatalyst and sonocatalyst due to its simple synthesis conditions, favorable optical band gap, and good chemical and thermal stability [8]. However, the rapid recombination of photo or sonogenerated electron–hole pairs on the catalyst limits both the photocatalytic and sonocatalytic performances of g-C_3N_4 [8]. Various strategies have been developed to obtain high photocatalytic and sonocatalytic performances with g-C_3N_4. Among the strategies, combining g-C_3N_4 with a carbon-based conductive filler can be considered an effective approach to reduce the recombination rate of photogenerated and sonogenerated charge carriers on g-C_3N_4, which can improve both the photocatalytic and sonocatalytic activity. Within this scope, carbon nanotubes [9], graphene [10], activated carbon [11], fullerene [12], graphene oxide [13] and carbon black [14] have been combined with g-C_3N_4 to enhance its photocatalytic activity, while only graphene oxide [15] as a carbon-based filler has been combined with g-C_3N_4 to improve its sonocatalytic activity in the literature.

The addition of carbon-based conductive fillers to the g-C_3N_4 structure promotes the separation and transport of mobile charge carriers on the catalyst, providing enhanced photocatalytic and sonocatalytic activity by g-C_3N_4 [14]. Among carbon-based fillers, carbon black is a type of paracrystalline carbon with a particle size smaller than 100 nm and a high surface area [14]. In general, carbon black has been preferred as a conductive filler for various applications due to its high stability and electrical conductivity. Carbon black could extend the lifetime of the photoexcited or sonoexcited electrons by forming the Schottky-based heterojunction structure on g-C_3N_4, thereby enhancing both photocatalytic and sonocatalytic activity [16]. In literature, Faisal and his coworkers (2022) confirmed that approximately 65% of the model organic pollutant was removed in the presence of pure g-C_3N_4. The photocatalytic removal rate was enhanced to 82% in the presence of polypyrrole coated carbon black/g-C_3N_4 composites within 25 min of visible light irradiation [17]. In another study, Wen and his coworkers (2015) investigated the effect of carbon black on the photocatalytic hydrogen production rate of g-C_3N_4/NiS composites. In addition to its charge separation effect, carbon black might enhance the visible light absorption property of g-C_3N_4, promoting the hydrogen production rate [18]. In a similar study, Wu and his coworkers (2014) increased the photocatalytic hydrogen production rate by 3.2 times by combining pure g-C_3N_4 with 0.5% by weight carbon black [19]. Guo and his coworkers (2023) prepared g-C_3N_4/carbon black/BiOBr-based photoanode for a visible light responsive fuel cell. It was observed that carbon black could not only promote the separation of the photoinduced charge carriers but also maintained the high reduction of the conduction band of g-C_3N_4, which was important

in terms of the photocatalytic activity of the catalyst [20].

In this study, g-C_3N_4/CB composites were prepared by a high-temperature treatment of waste melamine–formaldehyde in the presence of carbon black to prepare a catalyst for the photocatalytic or sonocatalytic degradation of tetracycline. The effect of the addition of carbon black into g-C_3N_4 on the chemical and physical structure and especially on the photocatalytic/sonocatalytic performance of g-C_3N_4 was studied. There are only a few studies in the literature on the photocatalytic performance of g-C_3N_4/CB composites, whereas there are no studies on the sonocatalytic activity of g-C_3N_4/CB composites. The novelty of this study was the synthesis of g-C_3N_4 from a waste material and the combination of g-C_3N_4 with carbon black in the composite structure for use as a photocatalyst/sonocatalyst for the removal of antibiotics from liquid media.

Experimental

Preparation of catalysts

Waste melamine–formaldehyde, including urea (15 wt%) and silica nanoparticles (10 wt%), was used to synthesize pure g-C_3N_4. A heat treatment was applied to the waste melamine–formaldehyde precursor in a Protherm model tube furnace (PTF Series, Thermo Scientific). The precursor was heated at a rate of 5°/min in an inert atmosphere until 650 °C, and the heating temperature was maintained at 650 °C for 4 h. Following the heat treatment process, silica nanoparticles, used as a template material, were removed from the g-C_3N_4 structure using diluted hydrofluoric acid, and the resulting powder was dried after the necessary cleaning and grinding processes. Therefore, pure g-C_3N_4 catalyst was obtained. It was also planned to obtain g-C_3N_4/CB composite catalysts with varying composition of carbon black (1, 2.5, 5, and 10 wt%). To prepare g-C_3N_4/CB composites, the same method applied for pure g-C_3N_4 synthesis was followed. Carbon black was added to the waste melamine–formaldehyde precursor before the heat treatment process. Following the physical mixing, waste melamine–formaldehyde/carbon black samples (including urea and silica nanoparticles) were subjected to the heat treatment under the same process conditions. Then, the as-prepared catalyst samples (g-C_3N_4/CB) were washed with hydrofluoric acid and distilled water, respectively, to get rid of the silica template material. Finally, g-C_3N_4/CB composite catalysts were obtained following the necessary drying and grinding processes. The as-prepared g-C_3N_4/CB sample was named g-C_3N_4/CB(x) (x = 1 wt%, 2.5 wt%, 5 wt%, and 10 wt% carbon black).

Characterization of catalysts

To verify the synthesis of pure g-C_3N_4 and g-C_3N_4/CB composites, Bruker IFS 66/S model FT-IR spectrometer was used to analyze the chemical structure and Rigaku Ultima IV model X-ray diffractometer to analyze the crystal structure. QUANTA 400 F model field emission scanning electron microscope was used to investigate the morphology of the catalyst samples. PHI 5000 VersaProbe model X-ray photoelectron spectrometer was used to analyze the surface chemical composition of the samples. Autosorb-6 model analyzer was used to measure the pore structure and the specific surface area by N_2 adsorption/desorption isotherms based on the Barret-Joyner-Halender (BJH) method and the Brunner–Emmett–Teller (BET) method, respectively. Jobin Yvon Flooring-550 Lumina model spectrophotometer was used to record the photoluminescence spectrum (PL) of the catalyst samples with an excitation wavelength of 350 nm. Genesys 10S model UV–Vis spectrophotometer was used to record UV–Vis absorbance spectroscopy of all catalyst samples.

Photocatalytic and sonocatalytic antibiotic degradation

The photocatalytic activity was evaluated by the degradation of a model antibiotic, tetracycline, under visible light irradiation. A 300 W (Osram Ultravitalux) visible light lamp was used as a light source. One hundred milligrams of catalysts was mixed with 100 mL of tetracycline solution (5 mg/L). After stirring the suspension in the dark for 30 min, the light source was turned on to start the photocatalytic degradation reaction. Two milliliters of the as-prepared suspension was sampled at specific time intervals and subjected to centrifugation to separate the liquid phase of the suspension. Genesys 10S model (Thermo Scientific) UV–Vis spectrophotometer was

used to evaluate the concentration of the sample solution at 358 nm.

The sonocatalytic activity of the catalyst samples was evaluated by the degradation of tetracycline under ultrasonic irradiation. One hundred milligram of the catalyst sample was dispersed into a 100 mL of tetracycline solution (5 mg/L). Before subjecting to ultrasonic irradiation, the as-prepared suspension was stirred for 30 min in the dark to achieve adsorption–desorption equilibrium. Then, the suspension was exposed to ultrasonic irradiation (20 kHz, 500 W) using 115 VAC model (Cole Parmar) ultrasonic homogenizer. A jacketed reactor with a water recirculation system was used to maintain the suspension temperature at around ambient temperature. Similar to the photocatalytic activity experiment, 2 mL sample was taken from the suspension at specific 20-min intervals during the sonocatalytic degradation process. Then, the tetracycline solution was separated from the catalyst powder through centrifugation. The tetracycline concentration was measured by using the UV–Vis spectrophotometer. The removal efficiency of tetracycline through the photocatalytic and sonocatalytic processes was calculated using Eq. (1) with UV–Vis absorption data of the tetracycline solution at 358 nm. In addition, the reaction kinetics of the tetracycline degradation through photocatalytic and sonocatalytic processes was evaluated using Eq. (2) based on the pseudo-first-order kinetic model [21]:

$$Tetracycline\ removal\ eff. = \frac{(C_0 - C)}{C_0} \quad (1)$$

$$ln\frac{C_0}{C} = kt \quad (2)$$

where C_0 represented the initial solution concentration of tetracycline, C denoted the final solution concentration of tetracycline, and k corresponded to the pseudo-first-order reaction rate constant [21].

Factors affecting the tetracycline removal efficiency were also investigated. The factors investigated were the initial solution concentration and the catalyst dosage. Within this scope, the initial solution concentration of tetracycline was varied from 1 to 10 mg/L, and the catalyst dosage of the tetracycline solution was varied from 0.5 to 1.5 g/L. To reveal the photocatalytic and sonocatalytic degradation mechanism of tetracycline over g-C_3N_4/CB(1), radical trapping experiments were performed. Two different radical scavengers, tert-butanol (60 mL/L) and ascorbic acid (10 mg/L), were added into the tetracycline solution, respectively, and the effect of the radical scavengers on the photocatalytic and sonocatalytic performance of g-C_3N_4/CB(1) was studied. To evaluate the reusability of the catalyst samples, g-C_3N_4/CB(1) was removed from the solution after the degradation reaction through centrifugation. Then, the catalyst powder was rinsed with distilled water and dried at 60 °C. The photocatalytic and sonocatalytic degradation of tetracycline over g-C_3N_4/CB(1) were repeated five times. To determine the adsorption capacity of g-C_3N_4/CB(1), 100 mg catalyst was added into 100 mL tetracycline solution (5 mg/L) with magnetic stirring in the dark. Two milliliter of the resulting suspension was sampled at a given time interval, and the sample suspension was centrifuged to separate the solid phase from the tetracycline solution. The adsorption capacity of g-C_3N_4/CB(1) was determined by recording the absorbance of the tetracycline solution with the UV–Vis spectrometer at 358 nm. The mineralization ratio of the tetracycline solution exposed to the ultrasonic irradiation or visible light irradiation was evaluated using a Shimadzu TOC-L (Japan) model total organic carbon (TOC) analyzer.

Results and discussion

Catalyst characterization

The XRD pattern of pure g-C_3N_4 is shown in Fig. 1(a). The pure sample exhibited characteristic diffraction peaks of g-C_3N_4 at $2\theta = 27.4°$ and 13.1°, which were assigned to the (002) plane and (100) plane, respectively (JCPDS 87–1526). The diffraction peak present at $2\theta = 27.4°$ might correspond to the interlayer stacking structure of polymer-conjugated aromatic rings, while the diffraction peak at $2\theta = 13.1°$ might be assigned to ordered repetition of the polymer unit [22]. In addition to the characteristic peaks of g-C_3N_4, there were additional peaks present at 17.1°, 34.4°, 36.2°, 39.4°, and 47.6° (Fig. 1(a)), attributed to the (1–10), (211), (023), (1–31), and (2–3-3) planes of melamine–formaldehyde, respectively (JCPDS 39–1950) [23, 24]. The additional peaks observed indicated the presence of unreacted melamine–formaldehyde in the

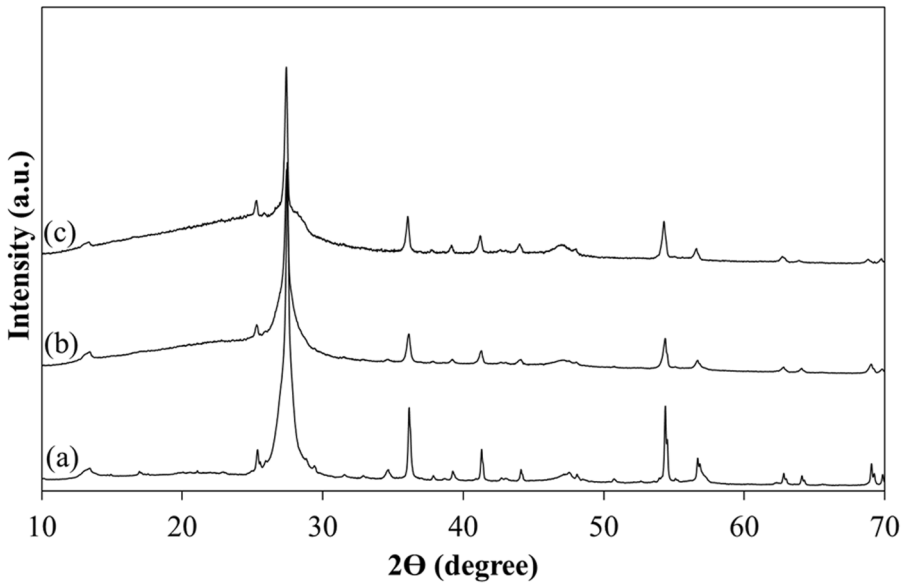

Fig. 1 XRD diffractogram of (**a**) g-C_3N_4, (**b**) g-C_3N_4/CB(1), and (**c**) g-C_3N_4/CB(5)

final product. Also, there were diffraction peaks at 48.6°, 62.8°, and 69.1°, referred to the (101), (110), and (112) planes of graphite. A certain amount of the melamine–formaldehyde precursor might be converted into the graphite phase during the heat treatment process [25]. The g-C_3N_4 samples incorporated with carbon black exhibited similar XRD patterns (Fig. 1(b) and 1(c)). Carbon black appeared to have negligible effects on the original crystal structure of g-C_3N_4. For the samples including carbon black, there was no shift for the characteristic peaks assigned to the (002) and (100) planes, indicating high dispersion of carbon black in g-C_3N_4 [18]. The similarity between the XRD patterns of pure and composite samples might be due to the very low concentration of carbon black in the composites. Similar XRD analysis results were also noticed in the study conducted by Hu and his coworkers [14]. On the other hand, a significant decrease in the intensity of non-g-C_3N_4 peaks was observed with the addition of carbon black, and this was attributed to the increased conversion efficiency of the precursor, melamine–formaldehyde, to g-C_3N_4. Carbon black might be stable during the heating process at 650 °C, and there might be no direct chemical reaction between carbon black and melamine–formaldehyde, resulting in no change in the XRD pattern of g-C_3N_4 [19]. A broad diffraction peak at about 25° was observed in the XRD patterns of both g-C_3N_4/CB(1) and g-C_3N_4/CB(5). This broad peak was attributed to an amorphous carbon structure formed due to carbon black [26]. It was observed that the peak intensity ratio of the plane (002) to the plane (100) for the composite samples was slightly lower than the peak intensity ratio observed for pure g-C_3N_4, which was attributed to an exfoliation process in the presence of carbon black [27]. The mean crystallite size (D) was calculated by using the Debye–Scherrer relation (3) [27]:

$$D = \frac{0.9\lambda}{\beta cos\theta} \tag{3}$$

at which λ is the wavelength of Cu Kα radiation, β is the full-width at half maximum of the most intense diffraction peak belonging to the (002) plane, and θ is the diffraction angle [27]. The average domain size for g-C_3N_4/CB(1) and g-C_3N_4/CB(5) calculated using the Debye–Scherrer relation was found to be 16.74 nm and 26.68 nm, respectively. Compared with g-C_3N_4 (25.11 nm), there was an insignificant change in the mean domain size with the addition of carbon black.

The characteristic functional groups of g-C_3N_4 were studied using FTIR spectroscopy (Fig. 2). Pure g-C_3N_4 and g-C_3N_4/CB(1) exhibited similar FTIR spectra. The transmittance peaks at around 1231 cm^{-1}, 1315 cm^{-1}, 1396 cm^{-1}, and 1460 cm^{-1} were attributed to the stretching vibration of the C-N single bond, while the transmittance peaks at

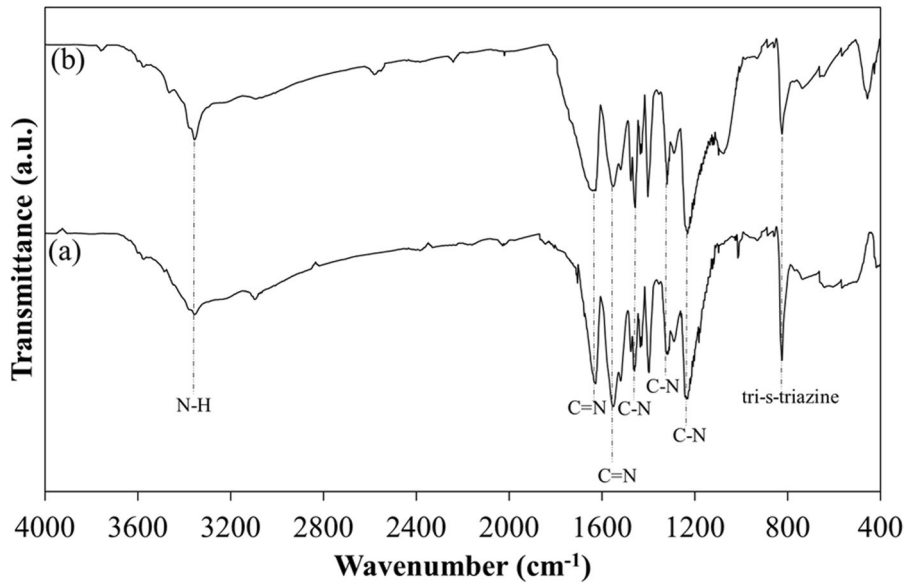

Fig. 2 FTIR spectrum of (**a**) g-C_3N_4 and (**b**) g-C_3N_4/CB(1)

around 1553 cm^{-1} and 1628 cm^{-1} were assigned to the stretching vibration of the C = N double bond [28]. The transmittance band at around 3300 cm^{-1} was attributed to the stretching vibration of the secondary N–H bond. In addition, the sharp transmittance peak at around 823 cm^{-1} was assigned to the characteristic tri-s-triazine cycles on g-C_3N_4 [28]. The FTIR spectra of both samples exhibited that the g-C_3N_4/CB sample retained the chemical structure of pure g-C_3N_4.

X-ray photoelectron spectroscopy (XPS) was performed to analyze the surface chemical composition of the catalyst samples. The full scan XPS spectra revealed the presence of carbon and nitrogen atoms for pure g-C_3N_4 and g-C_3N_4/CB(1) (Fig. 3a). The surface elemental compositions of both samples are illustrated in Table 1. The high-resolution C1s spectrum of g-C_3N_4 consisted of two peaks centered at 284.7 eV and 288.3 eV, attributed to sp2 carbon atoms of the graphitic carbon and sp2 carbon atoms bonded to aliphatic amine [14]. For g-C_3N_4/CB(1), the peak, assigned to the sp2 carbon atoms of the graphitic structure, was also observed at 284.7 eV, while the second peak, assigned to the sp2 carbon atoms bonded to aliphatic amine, was present at 288.2 eV (Fig. 3b). Compared with pure g-C_3N_4, there was a slight shift for the second peak in the high-resolution C1s spectrum of g-C_3N_4/CB(1). This shift in the peak position might be due to an interaction between carbon black and g-C_3N_4, resulting in a change in the chemical state of carbon atoms [14]. There was an additional peak at 286.7 eV in the XPS spectrum of g-C_3N_4/CB(1), which corresponded to the different oxidation state of carbon phase [14]. The high-resolution N1s spectrum of g-C_3N_4 consisted of two peaks at 398.8 eV and 400.9 eV (Fig. 3c), corresponding to sp2 nitrogen atoms in the aromatic C-N = C structure and sp3 nitrogen atoms in the N-$(C)_3$ group, respectively [27]. For g-C_3N_4/CB(1), the peak, attributed to the sp2 nitrogen atoms in the aromatic C-N = C structure, was observed at 398.8 eV, while the other peak, attributed to the sp3 nitrogen atoms in the N-$(C)_3$ group, was present at 400.6 eV (Fig. 3c). Compared with pure g-C_3N_4, there was a slight shift for the second peak in the high-resolution N1s spectrum of g-C_3N_4/CB(1).

The photoluminescence analysis has been used to investigate the recombination tendency of the photoexcited charged carriers on the catalyst. A lower photoluminescence intensity is a sign of a lower recombination rate of the photoexcited charge carriers, which could lead to higher photocatalytic performance [29]. The photoluminescence spectra of pure g-C_3N_4 and g-C_3N_4/CB(1) are compared in Fig. 4. Both of the catalyst samples exhibited similar photoluminescence curves. When compared with pure g-C_3N_4, g-C_3N_4/CB(1) revealed a lower photoluminescence intensity, attributed to the potential interaction between carbon black and g-C_3N_4 in the composite structure. The proposed interaction between the composite constituents

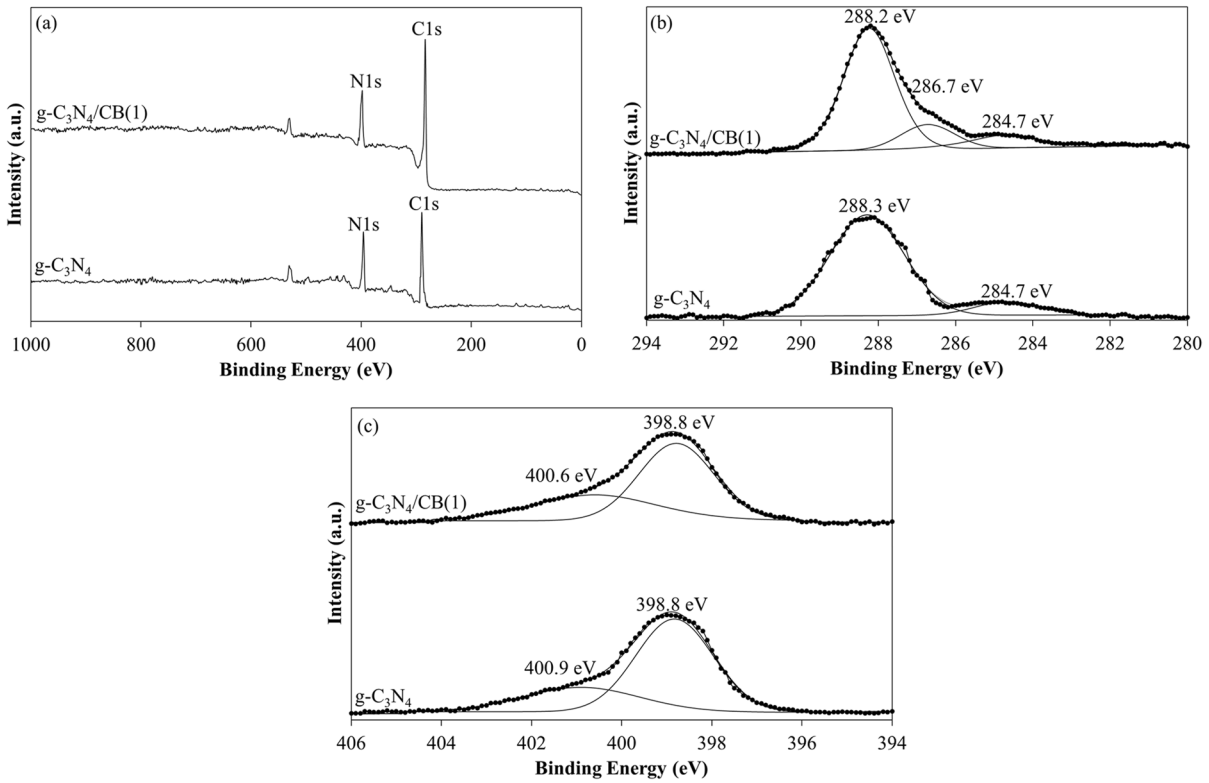

Fig. 3 XPS spectra of pure g-C_3N_4 and g-C_3N_4/CB(1): **a** full scan, **b** C1s, and **c** N1s

Table 1 Compositions of C, N, and O (wt%) in the samples obtained by the XPS analysis

Sample	C wt%	N wt%	O wt%
g-C_3N_4	66.2	27.3	6.5
g-C_3N_4/CB(1)	72.7	22.0	5.3

might promote the charge transfer on g-C_3N_4. Carbon black might act as trapping centers for the photoexcited electron–hole pairs or enhance the charge transfer due to its excellent conductivity, leading to a lower recombination rate of the photoexcited charge carriers.

The FESEM images of pure g-C_3N_4 and g-C_3N_4/CB composites are illustrated in Fig. 5. According to Fig. 5, irregular g-C_3N_4 particles with sizes of 300–600 nm were obtained from the melamine–formaldehyde precursor. Carbon black aggregates smaller than 100 nm might be dispersed among g-C_3N_4 particles. Considering the limited resolution of the FESEM images, it would not be appropriate to make a definitive statement about the dispersion of carbon black aggregates in the g-C_3N_4 matrix. The FESEM images were in good agreement with the morphology analysis reported in the literature by Wen and coworkers [18]. Compared to g-C_3N_4/CB(1), more carbon black aggregates were observed in FESEM images of g-C_3N_4/CB(5) (Fig. 5). It was observed that carbon black retained its structure during the heat treatment of the melamine–formaldehyde precursor to form g-C_3N_4.

The adsorption–desorption isotherms of pure g-C_3N_4 and g-C_3N_4/carbon black composites are shown in Fig. 6. All the N_2 adsorption–desorption isotherms seemed to be type IV, which indicated a mesoporous structure on the catalyst with a range of 2–50 nm mesopores. Additionally, the hysteresis loops of the N_2 adsorption–desorption isotherms were similar to the H3 type of hysteresis loops, indicating the presence of non-rigid aggregates of slit-like pores or plate-like particles with the catalyst [30]. The BET surface area and pore volume for g-C_3N_4/CB(1) and g-C_3N_4/CB(5) were larger compared to g-C_3N_4

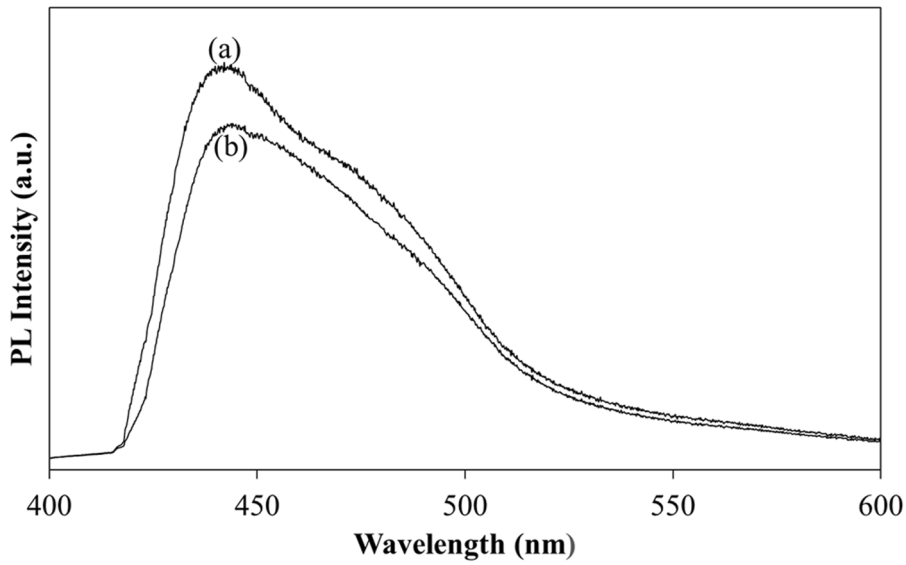

Fig. 4 The photoluminescence spectrum of (**a**) g-C_3N_4 and (**b**) g-C_3N_4/CB(1)

(Table 2). According to the BET results, g-C_3N_4 synthesized in the presence of carbon black might be less compact than pure g-C_3N_4, which was attributed to enhanced condensation of melamine in the presence of carbon black [31]. In addition, the BET surface area and the pore volume slightly increased with an increase in the carbon black content. On the other hand, carbon black is known as a porous material with a high specific surface area. Therefore, addition of carbon black might lead to a higher surface area and pore volume due to its porous structure [31]. The inset figure in the adsorption–desorption isotherm showed the corresponding BJH pore size distribution for each catalyst sample. Each sample exhibited a wide pore size distribution up to 50 nm (Fig. 6, inset). The wide pore size range in each sample could be advantageous in reducing the mass flow resistance of the adsorption/desorption of reactants and reaction products from the surface of the catalyst sample, thus increasing the tetracycline removal rate [32].

The UV–Vis absorption spectroscopy was performed to study the optical properties of pure and composite catalysts. The UV–Vis absorption spectrum of g-C_3N_4/CB(1), g-C_3N_4/CB(2.5), g-C_3N_4/CB(5), and g-C_3N_4/CB(10) exhibited a broad absorption band starting from 800 nm (Fig. 7). The light absorption behavior of g-C_3N_4/CB(1) and g-C_3N_4/CB(2.5) was different from the light absorption behavior of g-C_3N_4/CB(5) and g-C_3N_4/CB(10). As the carbon black content in the composite structure increased, carbon black behaved as the dominant phase in terms of the light absorption property. The spectrum of composite samples indicated a redshift compared to the spectrum of pure g-C_3N_4. In addition, a redshift was observed in parallel with the increase in the carbon black content in the composite structure. Figure S1 presents the Tauc plot for pure g-C_3N_4 and g-C_3N_4/CB composites. Combining g-C_3N_4 with carbon black in the composite structure narrowed the optical band gap. The optical band gap energy of pure g-C_3N_4, g-C_3N_4/CB(1), g-C_3N_4/CB(2.5), g-C_3N_4/CB(5), and g-C_3N_4/CB(10) was estimated to be 2.85 eV, 2.05, 1.80, 1.35, and 1.25 eV, respectively (Fig. S1).

Photocatalytic or sonocatalytic degradation of tetracycline molecules occurs on the surface of the catalyst. Therefore, the adsorption process has a crucial role in the occurrence of photocatalytic and sonocatalytic reactions and it is important to study the kinetics of the adsorption process [30]. The adsorption kinetics of pure g-C_3N_4 and g-C_3N_4/CB(1) were studied and their results are illustrated in Fig. 8. According to Fig. 8a, the adsorption capacity of both samples increased within 60 min, showed a slight increase until the 180th min, and then remained almost unchanged. For pure g-C_3N_4 and g-C_3N_4/CB(1), the maximum adsorption of tetracycline was achieved as 14.4% and 14.9%, respectively, after 240 min. The g-C_3N_4/CB(1) composite exhibited slightly stronger tetracycline adsorption ability compared to pure

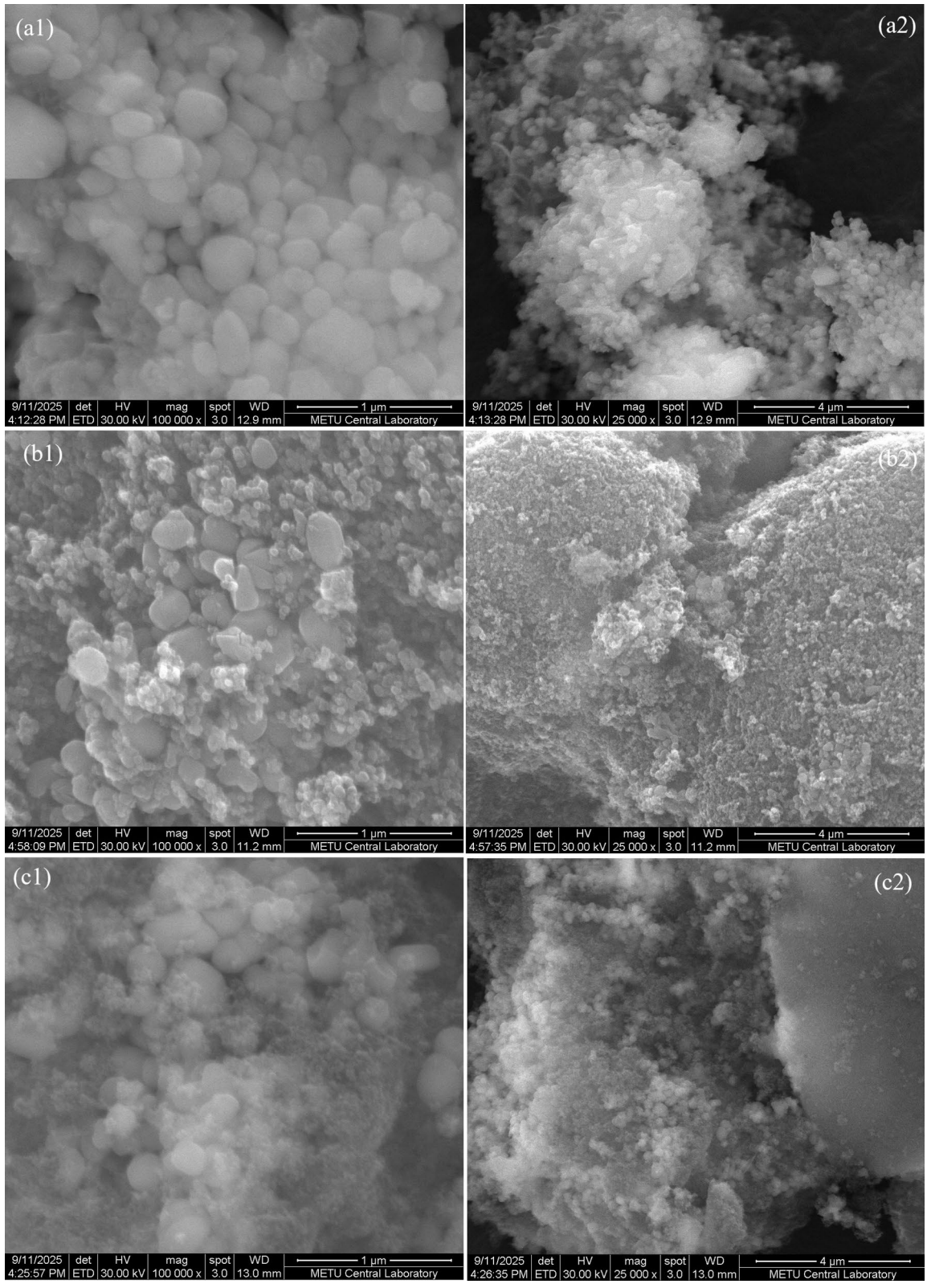
(a1)
9/11/2025 4:12:28 PM | det ETD | HV 30.00 kV | mag 100 000 x | spot 3.0 | WD 12.9 mm | 1 µm | METU Central Laboratory
(a2)
9/11/2025 4:13:28 PM | det ETD | HV 30.00 kV | mag 25 000 x | spot 3.0 | WD 12.9 mm | 4 µm | METU Central Laboratory
(b1)
9/11/2025 4:58:09 PM | det ETD | HV 30.00 kV | mag 100 000 x | spot 3.0 | WD 11.2 mm | 1 µm | METU Central Laboratory
(b2)
9/11/2025 4:57:35 PM | det ETD | HV 30.00 kV | mag 25 000 x | spot 3.0 | WD 11.2 mm | 4 µm | METU Central Laboratory
(c1)
9/11/2025 4:25:57 PM | det ETD | HV 30.00 kV | mag 100 000 x | spot 3.0 | WD 13.0 mm | 1 µm | METU Central Laboratory
(c2)
9/11/2025 4:26:35 PM | det ETD | HV 30.00 kV | mag 25 000 x | spot 3.0 | WD 13.0 mm | 4 µm | METU Central Laboratory

◂**Fig. 5** FESEM images of **a** g-C_3N_4, **b** g-C_3N_4/CB(1), and **c** g-C_3N_4/CB(5)

g-C_3N_4. which might be related to the larger specific surface area of carbon black and its composite with g-C_3N_4. The N_2 adsorption–desorption isotherms of pure g-C_3N_4 and g-C_3N_4/carbon black composites also confirmed it. The equilibrium adsorption capacity (q_e) of catalyst samples was obtained using the following relation [30]:

$$q_e\left(\frac{mg}{g}\right) = \frac{(C_0 - C_e)V}{m} \quad (4)$$

where C_0 and C_e are the initial and equilibrium concentration of tetracycline (mg/L), V is the volume of the antibiotic solution (L), and m is the weight of catalyst (g). As shown in Fig. 8b, the equilibrium adsorption amount of tetracycline was 1.441 mg/g and 1.489 mg/g on g-C_3N_4 and g-C_3N_4/CB(1), respectively.

The compatibility of the experimental adsorption data with the pseudo-first-order model and the pseudo-second-order model was also examined using the following relations [33]:

$$q_t = q_e\left(1 - e^{-k1t}\right) \quad (5)$$

$$q_t = \frac{k_2 {q_e}^2 t}{(1 + k_2 q_e t)} \quad (6)$$

where q_t (mg/g) and q_e (mg/g) are the amount of tetracycline adsorbed at the time (t) and at equilibrium, respectively, k_1 (min^{-1}) and k_2 (g/mg.min) are the pseudo-first-order and pseudo-second-order rate constant, respectively [33]. The adsorption data were fitted for the pseudo-first-order model by plotting the graph of ln (q_e-q_t) vs. t and for the pseudo-second-order model by plotting the graph of the t/q_t vs. t, and their results were illustrated in Fig. S2. The high correlation coefficient (R^2) indicated that the adsorption of tetracycline molecules on pure g-C_3N_4 and g-C_3N_4/CB(1) fitted almost perfectly to both the pseudo-first-order and pseudo-second-order models. On the other hand, if the experimental values of q_e were compared with the q_e values obtained from the pseudo-second-order kinetic model (Table 3), it was observed that the adsorption data were more in agreement with the pseudo-second-order model. In general, the pseudo-second-order model demonstrates that the adsorption mechanism of the catalyst sample is the main factor determining the adsorption capacity [33].

Photocatalytic and sonocatalytic tetracycline degradation

Figures S3 and S4 illustrate UV–Vis absorption spectra of tetracycline in the presence of pure g-C_3N_4 and g-C_3N_4/CB composites. Figure 9 exhibits photocatalytic and sonocatalytic antibiotic degradation efficiency of the as-prepared composite catalysts (g-C_3N_4/CB). The photocatalytic and sonocatalytic tetracycline degradation efficiency of pure g-C_3N_4 was 40.8% and 40.7%, respectively. g-C_3N_4/CB(10) exhibited relatively poor photocatalytic and sonocatalytic performances since only 38.2% of the tetracycline was decomposed within 120 min of visible light irradiation and only 37.8% of the tetracycline was removed from its solution after 120 min of ultrasonic irradiation. It was found that incorporating g-C_3N_4 with a high amount of carbon black was not effective in terms of photocatalytic and sonocatalytic performance because g-C_3N_4/CB(10) provided less photocatalytic and sonocatalytic performance compared to pure g-C_3N_4. On the other hand, the photocatalytic and sonocatalytic antibiotic degradation efficiency of g-C_3N_4/CB(1), g-C_3N_4/CB(2.5), and g-C_3N_4/CB(5) was much higher than that of pure g-C_3N_4. Furthermore, g-C_3N_4/CB(1) exhibited the highest photocatalytic and sonocatalytic tetracycline degradation efficiency. Almost 54.7% of the tetracycline was decomposed in the presence of g-C_3N_4/CB(1) after 120 min of visible light irradiation (Fig. 9a), while 53.4% of the tetracycline was removed from its solution within 120 min of ultrasonic irradiation (Fig. 9b). In particular, carbon black nanoparticles might act as an electron mediator by suppressing the recombination of photogenerated or sonogenerated electron–hole pairs on g-C_3N_4 and promoting the transfer of photoinduced/sonoinduced electrons from the bulk of the catalyst to its surface [9, 34]. The results showed that carbon black played an important role in improving both the photocatalytic and sonocatalytic performance of g-C_3N_4. However, the decrease in the photocatalytic/sonocatalytic activity of g-C_3N_4/carbon black with the increase in carbon black content

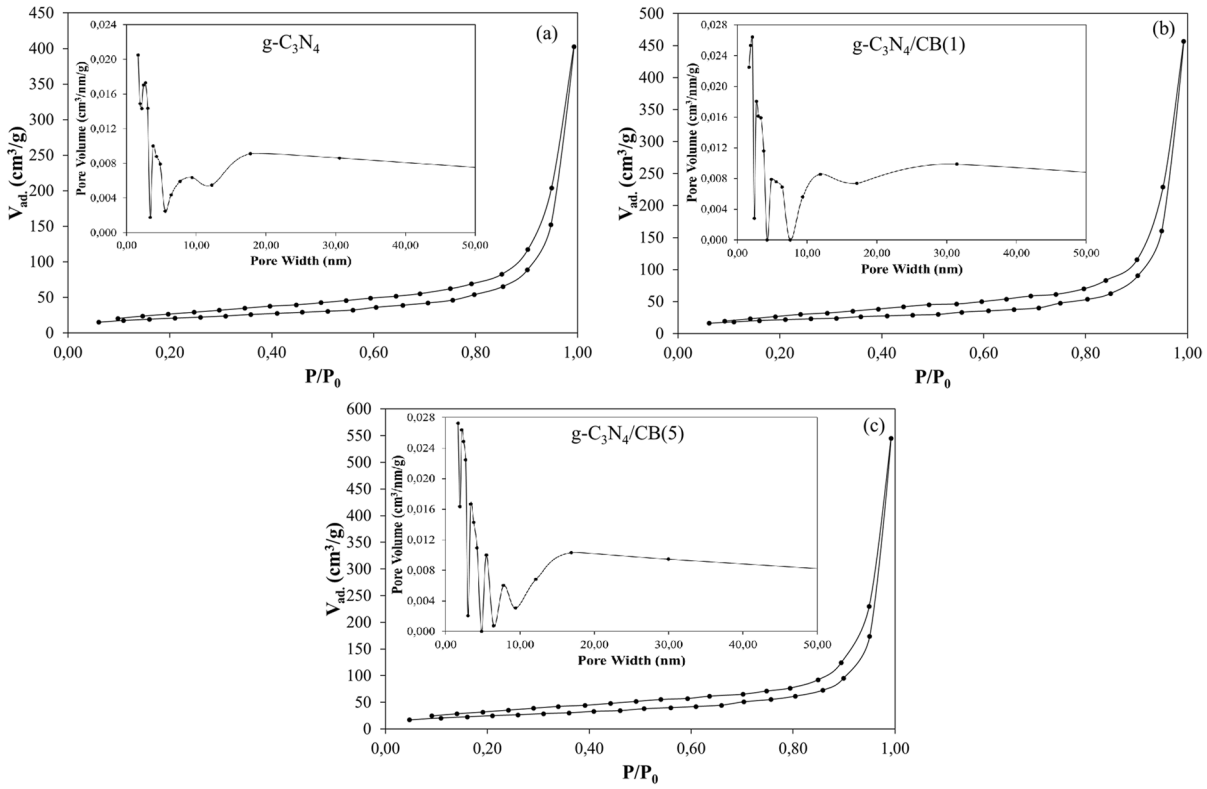

Fig. 6 N_2 adsorption–desorption isotherm (inset plots exhibit the BJH pore size distribution) for **a** g-C_3N_4, **b** g-C_3N_4/CB(1), and **c** g-C_3N_4/CB(5)

of the composite could be attributed to the shielding effect of carbon black [19].

In the presence of g-C_3N_4/CB(1), the degree of mineralization of antibiotic molecules in water was investigated by evaluating the total organic carbon (TOC) content [35]. After 120 min of sonocatalytic and photocatalytic tetracycline removal treatment, the TOC value of tetracycline mineralization was evaluated as 35.0% and 35.9% for g-C_3N_4/CB(1), respectively. The photocatalytic degradation process provided approximately the same total organic carbon (TOC) removal rate compared to the sonocatalytic process. Also, it was found that the mineralization rate of tetracycline at the end of sonocatalytic/photocatalytic processes was lower than the degradation rates of tetracycline after the sonocatalytic/photocatalytic processes. The difference between the mineralization rate and the degradation rate might stem from the fact that not all tetracycline molecules were completely mineralized and instead decomposed into smaller carbon-based products.

Table 2 Surface area and pore size data according to BET and BJH methods

Sample	BET surface area (m^2/g)	Pore volume (cm^2/g)	Average pore size (nm)
g-C_3N_4	73.69	0.634	1.68
g-C_3N_4/CB(1)	76.34	0.727	2.15
g-C_3N_4/CB(5)	89.17	0.857	1.65

The hybrid wastewater treatment techniques are beneficial to reduce the drawbacks of the individual process and to enhance the pollutant degradation efficiency. The hybrid treatment techniques can synergistically increase the number of reactive species in the reaction medium and improve the mass transfer in the liquid medium [36]. Within the scope of the hybrid treatment techniques, the photocatalytic and sonocatalytic degradation processes can be combined and applied as the sonophotocatalytic activity. The sonophotocatalytic tetracycline degradation efficiency of

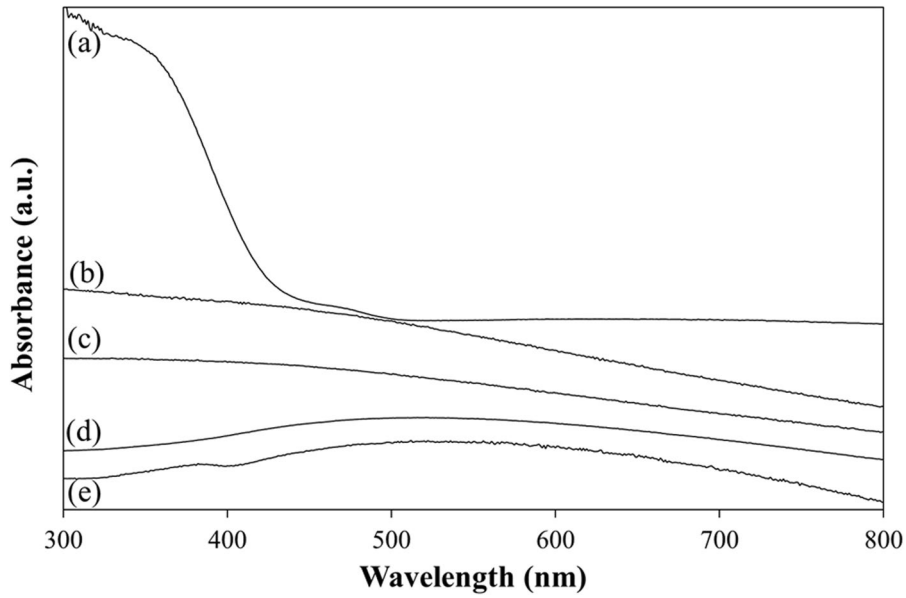

Fig. 7 UV–Vis absorbance spectrum of (**a**) g-C_3N_4, (**b**) g-C_3N_4/CB(1), (**c**) g-C_3N_4/CB(2.5), (**d**) g-C_3N_4/CB(5), and (**e**) g-C_3N_4/CB(10)

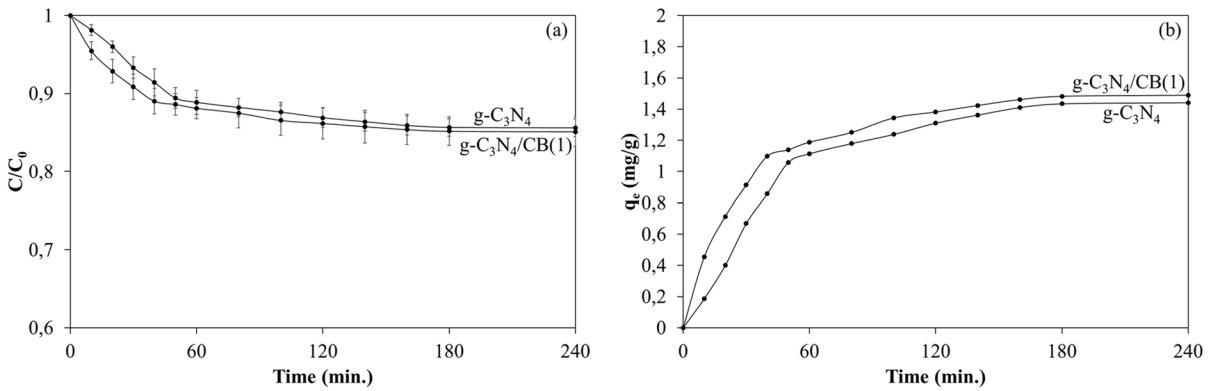

Fig. 8 **a** Adsorption efficiency and **b** adsorption kinetics of tetracycline over g-C_3N_4 and g-C_3N_4/CB(1)

Table 3 Parameters for the pseudo-first-order model and the pseudo-second-order model

Model	Sample	Experimental q_e (mg/g)	Calculated q_e (mg/g)	k_1(min^{-1})	k_2(g/mg.dk)	R^2
Pseudo-first-order	g-C_3N_4	1.4414	1.4698	0.0255	-	0.9430
	g-C_3N_4/CB(1)	1.4894	0.9006	0.0250	-	0.9535
Pseudo-second-order	g-C_3N_4/	1.4414	1.8893	-	0.0093	0.9582
	g-C_3N_4/CB(1)	1.4894	1.6631	-	0.0248	0.9990

g-C_3N_4/CB composites was slightly higher than the photocatalytic degradation efficiency and sonocatalytic degradation efficiency of g-C_3N_4/CB. After the combined application of the ultrasonic irradiation and visible light irradiation, the tetracycline removal rates on g-C_3N_4/CB(1), g-C_3N_4/CB(2.5), g-C_3N_4/CB(5), and g-C_3N_4/CB(10) were 59.8%, 58.5%, 51.1%, and 44.1%, respectively (Fig. 9c). As expected, the

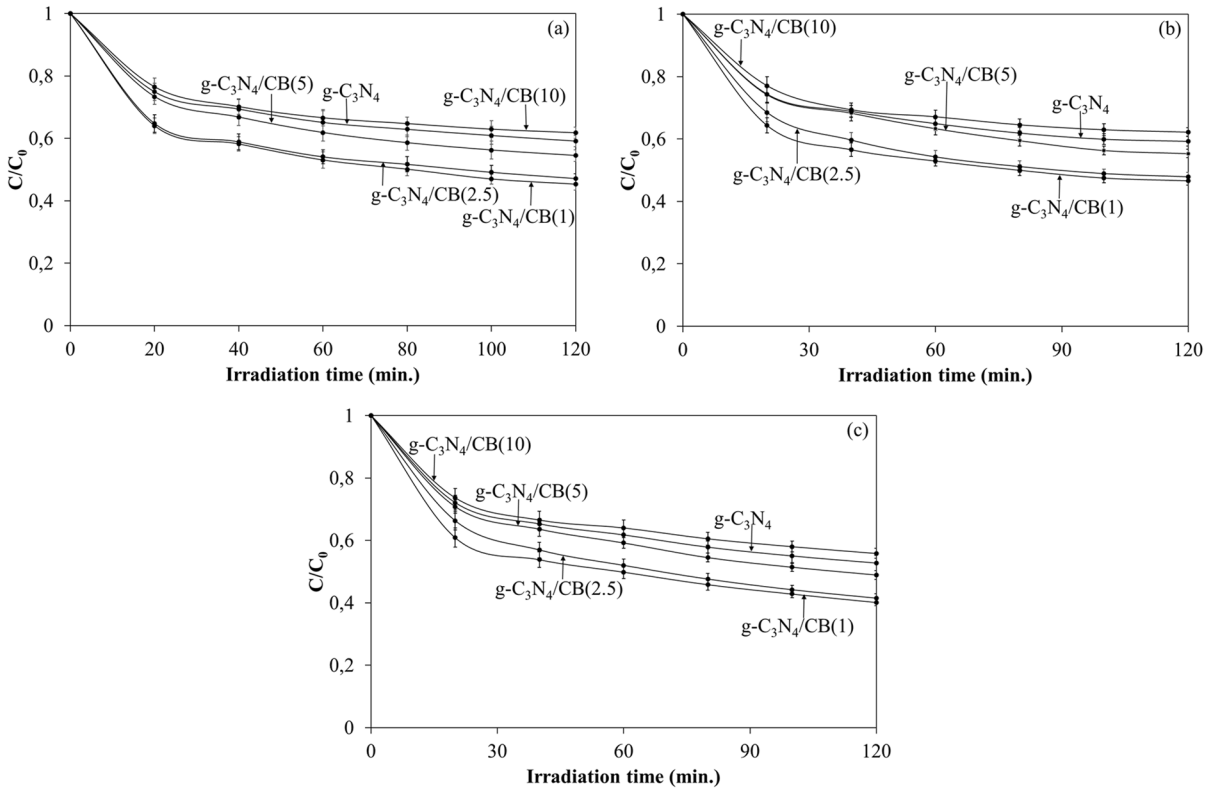

Fig. 9 C/C_0 plots of g-C_3N_4, g-C_3N_4/CB(1), g-C_3N_4/CB(2.5), g-C_3N_4/CB(5), and g-C_3N_4/CB(10) subjected to **a** photocatalytic, **b** sonocatalytic, and **c** sonophotocatalytic tetracycline degradation

ultrasonic irradiation and the visible light irradiation together promoted the tetracycline degradation efficiency. The improvement in tetracycline removal efficiency might be related to the continuous cleaning of the catalyst surface, increased mass transfer of tetracycline molecules and reactive species, and an increase in the number of active radicals [36]. In addition, the simultaneous application of photocatalytic and sonocatalytic activity could enhance the dispersion of tetracycline molecules in its solution [36].

To better understand the photocatalytic and sonocatalytic performance of g-C_3N_4/carbon black composites, tetracycline degradation kinetics was also investigated. The tetracycline degradation was attempted to be fitted to a pseudo-first-order reaction kinetics model (Fig. S5). The reaction rate constant value for the photocatalytic tetracycline degradation was calculated as 0.0083 min^{-1}, 0.008 min^{-1}, 0.0063 min^{-1}, 0,0052 min^{-1} for g-C_3N_4/CB(1), g-C_3N_4/CB(2.5), g-C_3N_4/CB(5), and g-C_3N_4/CB(10),

Table 4 Adjusted parameters of the pseudo-first-order kinetic model

	Photocatalytic		Sonocatalytic		Sonophotocatalytic	
Sample	k (min^{-1})	R^2	k (min^{-1})	R^2	k (min^{-1})	R^2
g-C_3N_4	0.0054	0.5696	0.0055	0.5531	0.0064	0.6552
g-C_3N_4/CB(1)	0.0081	0.5762	0.0080	0.5056	0.0091	0.6036
g-C_3N_4/CB(2.5)	0.0077	0.5299	0.0077	0.6130	0.0087	0.7200
g-C_3N_4/CB(5)	0.0062	0.6507	0.0060	0.6859	0.0071	0.7148
g-C_3N_4/CB(10)	0.0050	0.5289	0.0050	0.5177	0.0059	0.6108

respectively (Table 4), while the reaction rate constant value for the sonocatalytic tetracycline degradation was calculated as 0.0080 min^{-1}, 0.0077 min^{-1}, 0.0060 min^{-1}, and 0.0050 min^{-1} for g-C_3N_4/CB(1), g-C_3N_4/CB(2.5), g-C_3N_4/CB(5), and g-C_3N_4/CB(10), respectively. The results revealed that combining g-C_3N_4 with carbon black within the composite structure enhanced the tetracycline degradation rate of g-C_3N_4. Compared to pure g-C_3N_4, a 1.5-fold increase in the reaction rate of the photocatalytic tetracycline degradation was obtained with the g-C_3N_4/CB(1) composite, revealing the positive effect of the conductive carbon-based filler on the photocatalytic performance of g-C_3N_4. When compared with pure g-C_3N_4, an almost 1.5-fold increase in the reaction rate of the sonocatalytic antibiotic degradation was obtained with the g-C_3N_4/CB(1) composite. The reaction rate constants for the sonophotocatalytic reactions were slightly higher than those for the sonocatalytic and photocatalytic reactions, indicating that g-C_3N_4/carbon black samples provided higher tetracycline removal rates through sonophotocatalytic reactions (Fig. S5).

The synergy index for degradation of tetracycline was calculated using the following relation [36]:

$$Synergetic - index = \frac{k_{\text{Sonophotocatalysis}}}{k_{\text{Photocatalysis}} + k_{\text{Sonophotocatalysis}}} \quad (7)$$

where k was the pseudo-first-order reaction rate constant. The degradation efficiency of the sonophotocatalytic process could not exceed the sum of individual processes, indicating a synergistic effect of almost 0.6 for the sonophotocatalytic degradation reaction. The synergy index was smaller than 1.0, indicating that combining the two treatment processes did not appear feasible in terms of tetracycline removal efficiency.

Effect of catalyst dosage and initial solution concentration

The effect of the catalyst dosage on the photocatalytic and sonocatalytic activity is illustrated in Fig. 10. When the catalyst dosage was increased from 0.5 to 1.25 g/L, the photocatalytic tetracycline degradation efficiency increased from 49.8 to 57.7%, revealing that the number of active sites on the catalyst controlled the degradation reaction rate [37]. Further increasing the catalyst dose could not improve the photocatalytic degradation efficiency of tetracycline [37]. An excess of catalyst could affect the penetration of visible light photons into the reaction medium and prevent some catalysts from being sufficiently excited by the visible light [37]. Unlike the photocatalytic process, the sonocatalytic tetracycline degradation efficiency of g-C_3N_4/CB(1) enhanced as the catalyst dosage increased from 0.5 to 1.5 g/L.

The initial solution concentration of the pollutant molecules is also important in terms of the photocatalytic and sonocatalytic performance of catalysts. As the initial solution concentration of tetracycline increased from 1 to 7.5 mg/L, both the photocatalytic and sonocatalytic tetracycline removal efficiency improved (Fig. 11). As the photocatalytic tetracycline degradation efficiency of g-C_3N_4/CB(1) increased

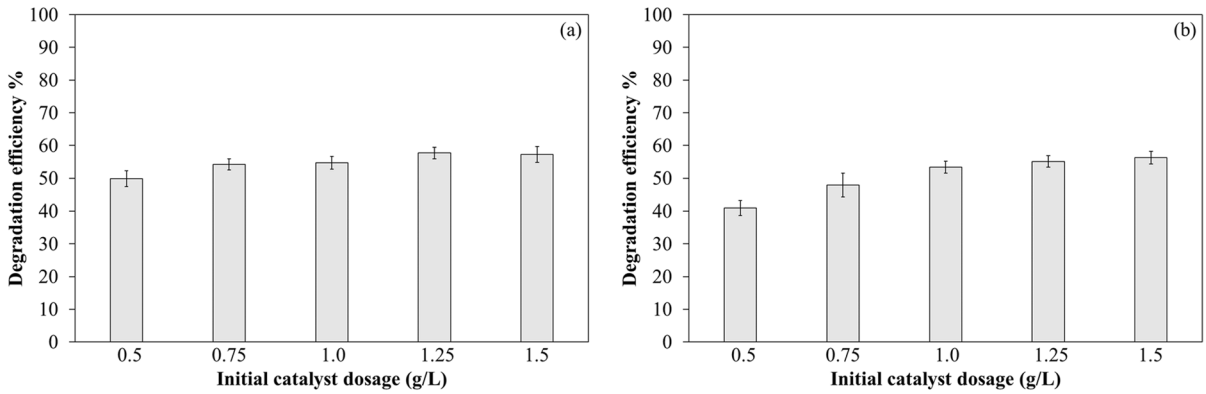

Fig. 10 Effect of catalyst dosage on **a** photocatalytic and **b** sonocatalytic degradation of tetracycline over g-C_3N_4/CB(1)

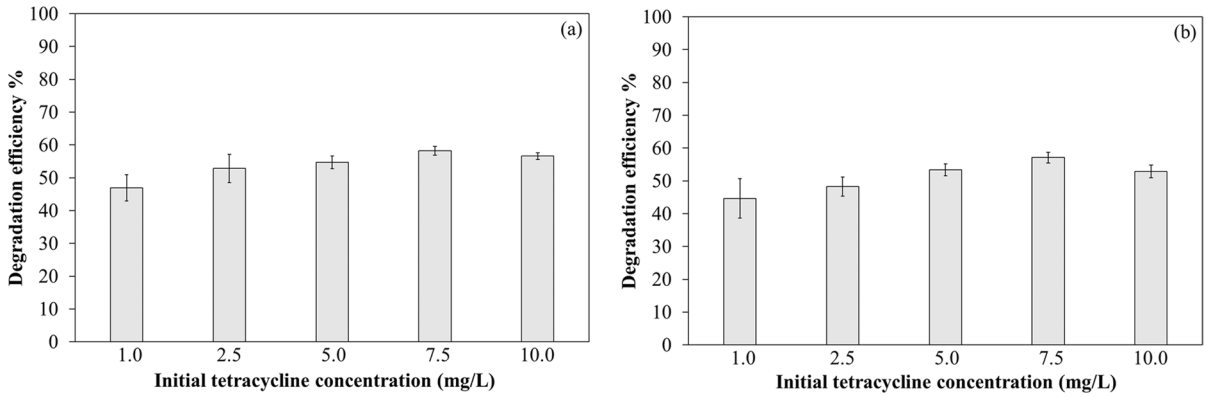

Fig. 11 Effect of initial tetracycline concentration on **a** photocatalytic and **b** sonocatalytic degradation of tetracycline over g-C_3N_4/CB(1)

from 46.9 to 58.2%, the sonocatalytic tetracycline removal efficiency increased from 44.6 to 57.1%. An excess of the initial solution concentration of tetracycline decreased both the photocatalytic and sonocatalytic removal efficiency, which was attributed to the limited number of active sites on the catalyst surface [37].

Effect of scavengers

To determine the active radicals responsible for the photocatalytic and sonocatalytic degradation of tetracycline, radical trapping experiments were performed. Figure 12 exhibits the photocatalytic degradation efficiency of tetracycline by g-C_3N_4/CB(1) in the presence of two different scavengers added into the reaction medium. It was observed that the addition of ascorbic acid significantly reduced the photocatalytic removal rate of tetracycline, indicating that superoxide radicals played a major role in the photocatalytic degradation reactions. On the other hand, the addition of tert-butanol slightly reduced the photocatalytic degradation efficiency of tetracycline, indicating that hydroxyl radicals played a secondary role in the photocatalytic degradation reactions. As shown in Fig. 12, the sonocatalytic degradation efficiency of

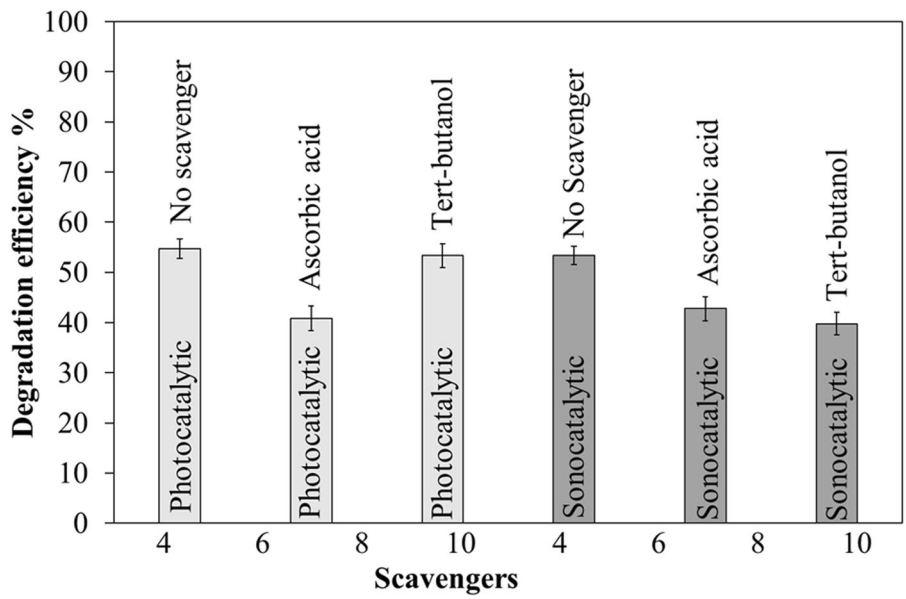

Fig. 12 The photocatalytic and sonocatalytic tetracycline removal efficiency over g-C_3N_4/CB(1) in the presence of radical scavengers

tetracycline decreased from 53.4 to 42.7% in the presence of ascorbic acid. When tert-butanol was added into the reaction medium, the sonocatalytic tetracycline degradation efficiency reduced to 39.8%, indicating that both the superoxide and hydroxyl radicals played significant roles for the sonocatalytic degradation of tetracycline over g-C_3N_4/CB(1).

In their previous studies, the researchers of this study calculated the edge potentials of the conduction band and valence band for g-C_3N_4 as −1.20 eV and 1.65 eV, respectively [38]. Both the visible light and sonoluminescence induced by ultrasonic irradiation could excite the valence band electrons of g-C_3N_4 to form photogenerated and sonogenerated electron–hole pairs. The standard reduction potential of O_2 to form superoxide radicals was more positive than the conduction band edge potential of g-C_3N_4, while the standard oxidation potential of H_2O to form hydroxyl radicals was also more positive than the valence band edge potential of g-C_3N_4. Therefore, the conduction band edge potential of g-C_3N_4 was favorable for the formation of superoxide radicals on the catalyst surface, whereas the valence band edge potential of g-C_3N_4 was unfavorable for the formation of hydroxyl radicals [39, 40]. Hence, superoxide radicals should be the main active radical for both the photocatalytic and sonocatalytic degradation of tetracycline. The radical trapping experiments supported the proposed degradation mechanism for the photocatalytic activity.

However, the radical trapping experiments revealed that both superoxide and hydroxyl radicals were the main active radicals for the sonocatalytic degradation of tetracycline. The presence of a catalyst in an ultrasonic system might lead to the formation of hydroxyl radicals in the irradiated medium. The formation of hydroxyl radicals could be explained by hot spots formation. Due to heterogeneous nucleation of bubbles on g-C_3N_4/CB, the number of cavitation bubbles might increase, leading to the formation of hot spots in the solution. The resulting hot spots might convert water molecules into hydroxyl radicals, which could facilitate the degradation of tetracycline. The source of hydroxyl radicals, which were active during the sonocatalytic degradation reactions, might be the formation of hot spots [41].

Reusability of catalysts

The reusability of g-C_3N_4/CB as a photocatalyst or sonocatalyst was also an important aspect of this study. This is important because it directly affects the economic feasibility of its application in wastewater treatment processes. After each photocatalytic or sonocatalytic run, the catalyst powder was removed from the reaction medium by centrifugation, rinsed with distilled water, and then dried. Figure 13 illustrates that both the photocatalytic and sonocatalytic degradation efficiency of tetracycline over g-C_3N_4/CB(1) slightly reduced after five consecutive degradation cycles. The photocatalytic tetracycline degradation efficiency reduced from 54.7 to 43.9%, while the sonocatalytic tetracycline removal rate reduced from 53.4 to 43.0%, indicating robust structural integrity of the composite catalyst and minimal removal of carbon black from the

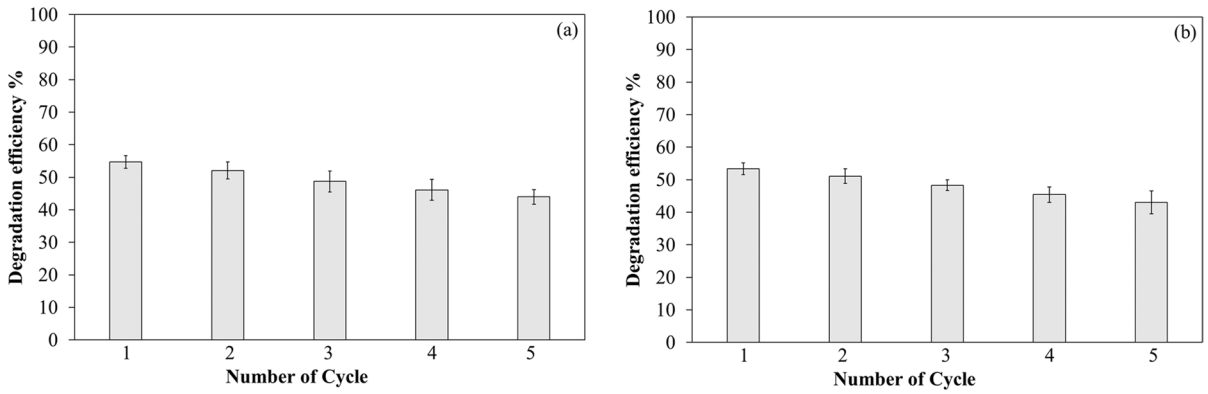

Fig. 13 Repetitive cycles of **a** photocatalytic and **b** sonocatalytic tetracycline degradation over g-C_3N_4/CB(1)

g-C_3N_4 matrix [42]. The strong interaction between g-C_3N_4 and carbon black might provide a stable platform and inhibit the removal of carbon black during the photocatalytic and sonocatalytic degradation processes, minimizing the catalyst loss [42].

Conclusions

The g-C_3N_4/CB composites were successfully synthesized through a heat treatment process using a waste melamine–formaldehyde precursor. The N_2 adsorption/desorption analyses exhibited that g-C_3N_4/CB had a larger specific surface area and pore volume, providing more active sites for adsorption of tetracycline molecules. But, the adsorption capacity of tetracycline on g-C_3N_4/CB(1) increased slightly from 1.441 to 1.489 mg/g under 240 min dark condition. The adsorption behaviors of pure g-C_3N_4 and g-C_3N_4/CB(1) were consistent with the pseudo-second-order kinetic model. The morphology analysis exhibited that carbon black aggregates were uniformly dispersed in the g-C_3N_4 matrix, promoting the charge separation on g-C_3N_4. The tetracycline removal efficiency of g-C_3N_4/CB(1) by the photocatalytic process and sonocatalytic process reached 54.7% and 53.4%, respectively, after 120 min. The enhanced photocatalytic and sonocatalytic performance was attributed to the suppressed recombination of charge carriers on g-C_3N_4 owing to the conductive pathway of carbon black. The radical trapping experiments demonstrated that superoxide radicals played a major role for the photocatalytic degradation of tetracycline, whereas both superoxide and hydroxyl radicals were important in terms of the sonocatalytic performance of g-C_3N_4/CB catalysts.

Acknowledgements The authors are thankful to The Scientific and Technological Research Council of Türkiye (TÜBİTAK) for the research grant 224M345.

Author contribution All authors contributed to the study conception and design. Material preparation, data collection and analysis were performed by Hafize Nagehan Koysuren, Sumyah Amer Yahya and Ozcan Koysuren.

Funding Open access funding provided by the Scientific and Technological Research Council of Türkiye (TÜBİTAK). This research has been supported by The Scientific and Technological Research Council of Türkiye (TÜBİTAK) with the Project Number 224M345.

Data availability The datasets generated during and/or analyzed during the current study are available from the corresponding author on reasonable request.

Declarations

Competing interests The authors declare no competing interests.

References

1. Zhou H, Jiang S, Wang X, Zhi X, Zhang Z, Li X, Tai Y, Xu X (2025) Polydopamine-modified g-C3N4/TiO2/GO PVDF membranes for enhanced quinolone antibiotic photocatalytic removal. J Water Process Eng 76:108280. https://doi.org/10.1016/j.jwpe.2025.108280
2. John KI, Ho G, Li D (2024) Recent progresses in synthesis and modification of g-C3N4 for improving visible-light-driven photocatalytic degradation of antibiotics. Water Sci Technol 89(11):3047–3078. https://doi.org/10.2166/wst.2024.166
3. Liu C, Zhu X, Wang L, Feng C, Rong J, Li Z, Xu S (2024) Construction of NiTiO3/g-C3N4 heterojunction with preferable photocatalytic performance for tetracycline degradation. J Solid State Chem 339:124953. https://doi.org/10.1016/j.jssc.2024.124953
4. Guo Y, Li J, Zhang J, Wang X (2024) Highly active BiFeO3–g-C3N4 S-scheme heterojunction with improved antibiotic degradation under visible-light: revealing mechanism. Res Chem Intermed 50(8):3505–3521. https://doi.org/10.1007/s11164-024-05326-1
5. Zhang H, Qiao J, Li G, Li S, Wang G, Wang J, Song Y (2018) Preparation of Ce4+-doped BaZrO3 by hydrothermal method and application in dual-frequent sonocatalytic degradation of norfloxacin in aqueous solution. Ultrason Sonochem 42:356–367. https://doi.org/10.1016/j.ultsonch.2017.11.043
6. Teng J, Xiong S, Li F, Wang S, Li T (2024) Sonocatalytic performance of Bi2WO6 nanoparticles for degradation

of tetracycline antibiotics. Applied Catalysis O: Open 191:206957. https://doi.org/10.1016/j.apcato.2024.206957
7. Nejat R, Zandi S (2025) Visible-light responsive $La_{0.7}Sr_{0.3}MnO_3$@TiO_2/g-C_3N_4 nanocomposite for photocatalytic antibiotic degradation and bioactivity applications. J Alloys Compd. https://doi.org/10.1016/j.jallcom.2025.181866
8. Narzary M, Wary RR, Brahma BB, Kalita P, Baruah MB (2025) Oxygen vacancy mediated Zn3V2O8/g-C3N4 direct Z-scheme heterojunction for enhanced visible light photocatalytic degradation of organic dye and broad-spectrum antibiotic. J Alloys Compd. https://doi.org/10.1016/j.jallcom.2025.182598
9. Wang W, Wang L, Li W, Feng C, Qiu R, Xu L, Cheng X, Shao G (2019) Fabrication of a novel g-C3N4/Carbon nanotubes/Ag3PO4 Z-scheme photocatalyst with enhanced photocatalytic performance. Mater Lett 234:183–186. https://doi.org/10.1016/j.matlet.2018.09.098
10. Yang X, Tian Z, Chen Y, Huang H, Hu J (2020) One-pot calcination preparation of graphene/g–C3N4–Co photocatalysts with enhanced visible light photocatalytic activity. Int J Hydrogen Energy 45(23):12889–12902. https://doi.org/10.1016/j.ijhydene.2020.03.028
11. Feng P, Cui K, Hai Z, Wang J, Wang L (2023) Facile synthesis of activated carbon loaded g-C3N4 composite with enhanced photocatalytic performance under visible light. Diamond Relat Mater 136:109921. https://doi.org/10.1016/j.diamond.2023.109921
12. Bai X, Wang L, Wang Y, Yao W, Zhu Y (2014) Enhanced oxidation ability of g-C3N4 photocatalyst via C60 modification. Appl Catal B 152:262–270. https://doi.org/10.1016/j.apcatb.2014.01.046
13. Wang YX, Chen MN, Tao H (2020) Preparation of nested g-C3N4 fiber surrounding graphene oxide and its photocatalytic degradation of rhodamine B. J Nanosci Nanotechnol 20(9):5445–5451. https://doi.org/10.1166/jnn.2020.17880
14. Hu S, Wang H, Wang F, Bai J, Zhang L, Kang X, Wu G (2015) Practical preparation of carbon black/carbon nitride compounds and their photocatalytic performance. Bull Korean Chem Soc 36(10):2527–2533. https://doi.org/10.1002/bkcs.10491
15. Gak JCD, Mohamed MM, Ibrahim I, Matsushita Y, Mawgood AA (2024) Efficient sonocatalytic degradation of pyrene using a novel and magnetically recoverable graphitic carbon nitride–cobalt ferrite–graphene oxide (g-C3N4/CoFe2O4@ GO) nanocomposite with an enhanced Z-scheme electron transfer pathway. Ceram Int 50(18):34431–34441. https://doi.org/10.1016/j.ceramint.2024.06.262
16. Shen R, Liu W, Ren D, Xie J, Li X (2019) Co1.4Ni0.6P cocatalysts modified metallic carbon black/g-C3N4 nanosheet Schottky heterojunctions for active and durable photocatalytic H2 production. Appl Surf Sci 466:393–400. https://doi.org/10.1016/j.apsusc.2018.10.033
17. Faisal M, Rashed MA, Ahmed J, Alsaiari M, Jalalah M, Alsareii SA, Harraz FA (2022) Au nanoparticles decorated polypyrrole-carbon black/g-C3N4 nanocomposite as ultrafast and efficient visible light photocatalyst. Chemosphere 287:131984. https://doi.org/10.1016/j.chemosphere.2021.131984
18. Wen J, Li X, Li H, Ma S, He K, Xu Y, Fang Y, Liu W, Gao Q (2015) Enhanced visible-light H2 evolution of g-C3N4 photocatalysts via the synergetic effect of amorphous NiS and cheap metal-free carbon black nanoparticles as co-catalysts. Appl Surf Sci 358:204–212. https://doi.org/10.1016/j.apsusc.2015.08.244
19. Wu Z, Gao H, Yan S, Zou Z (2014) Synthesis of carbon black/carbon nitride intercalation compound composite for efficient hydrogen production. Dalton Trans 43(31):12013–12017. https://doi.org/10.1039/C4DT00256C
20. Guo H, Yu T, Zhao L, Qian J, Yu J, Zhang Y, Teng Y, Zhu C, Yang T, Chen W, Gong P (2023) Performance study of g-C3N4/carbon black/BiOBr@ Ti3C2/MoS2 photocatalytic fuel cell for the synergistic degradation of different types of pollutants. Carbon Lett 33(3):847–862. https://doi.org/10.1007/s42823-023-00465-8
21. Vu VP, Le Na NT, Luong MT, Toan ND, Thi NAT, Nguyen TT, Hoang MH, Nguyen LD, Dao KL, Nguyen TB, Sai CD (2025) Visible light-driven GO/Ag-ZnO ternary composites for enhanced photocatalytic degradation of amoxicillin and their antibacterial potential. Next Materials 8:100544. https://doi.org/10.1016/j.nxmate.2025.100544
22. Yang H, Gong Y, Yang P, Zhong J, Li J (2025) Photocatalytic CO2 reduction over carbon vacancies enriched g-C3N4 treated by NaClO. Chem Phys Lett. https://doi.org/10.1016/j.cplett.2025.142153
23. Islam MR, Chakraborty AK, Gafur MA, Rahman MA, Rahman MH (2019) Easy preparation of recyclable thermally stable visible-light-active graphitic-C3N4/TiO2 nanocomposite photocatalyst for efficient decomposition of hazardous organic industrial pollutants in aqueous medium. Res Chem Intermed 45(4):1753–1773. https://doi.org/10.1007/s11164-018-3703-7
24. Bhosale RS, Al Kobaisi M, Bhosale SV, Bhargava S, Bhosale SV (2015) Flower-like supramolecular self-assembly of phosphonic acid appended naphthalene diimide and melamine. Sci Rep 5(1):14609. https://doi.org/10.1038/srep14609
25. Ban FY, Majid SR, Huang NM, Lim HN (2012) Graphene oxide and its electrochemical performance. Int J Electrochem Sci 7(5):4345–4351. https://doi.org/10.1016/S1452-3981(23)19543-5
26. Wen J, Xie J, Yang Z, Shen R, Li H, Luo X, Chen X, Li X (2017) Fabricating the robust g-C3N4 nanosheets/carbons/NiS multiple heterojunctions for enhanced photocatalytic H2 generation: an insight into the trifunctional roles of nanocarbons. ACS Sustain Chem Eng 5(3):2224–2236. https://doi.org/10.1021/acssuschemeng.6b02490
27. Parga B, Ruiz-Gómez MA, Rodríguez-González V, Vázquez A, Obregón S (2025) Nitrogen-rich g-C3N4 synthesized by simultaneous melamine/urea polycondensation for photocatalytic removal of tetracycline hydrochloride. Materials Today Communications. https://doi.org/10.1016/j.mtcomm.2025.114258
28. Kim KS, Choi SY, Kim TW, Kang MJ (2024) Recycling waste melamine-formaldehyde resin as a photocatalytic enhancer for g-C3N4 photocatalysts and application in

photoelectrochemical (PEC) reactions. ACS Sustain Chem Eng 12(18):7083–7091. https://doi.org/10.1021/acssuschemeng.4c00748
29. Gul I, Sayed M, Rehman F, Jinlong W, Fu P, Zhang Y, Nadagouda MN (2025) Z-scheme Ti3C2@ Bi2O3 based MXene with multifaceted (0 0 1) and (1 0 1) TiO2 and Ti3+/oxygen vacancies: photocatalytic degradation of dichlorophen via peroxymonosulfate activation, energy utilization and antibacterial activities. Chem Eng J 506:159992. https://doi.org/10.1016/j.cej.2025.159992
30. Saadati A, Sheibani S (2022) Insight into the adsorption and photocatalytic properties of in-situ synthesized g-C3N4/SnS2 nanocomposite. Ceram Int 48(20):30294–30306. https://doi.org/10.1016/j.ceramint.2022.06.302
31. Zhang L, Jin Z, Lu H, Lin T, Ruan S, Zhao XS, Zeng YJ (2018) Improving the visible-light photocatalytic activity of graphitic carbon nitride by carbon black doping. ACS Omega 3(11):15009–15017. https://doi.org/10.1021/acsomega.8b01933
32. Gul I, Sayed M, Rehman F, Jinlong W, Fu P, Zhang Y, Nadagouda MN (2024) Unlocking the potential of multifunctional and highly porous Ti3C2/TiO2@ Bi2O3–based MXene: synergetic photocatalytic activation of peroxymonosulfate, hydrogen evolution and antimicrobial activity. Appl Catal B Environ Energy 359:124493. https://doi.org/10.1016/j.apcatb.2024.124493
33. Shi J, Chen T, Guo C, Liu Z, Feng S, Li Y, Hu J (2019) The bifunctional composites of AC restrain the stack of g-C3N4 with the excellent adsorption-photocatalytic performance for the removal of RhB. Colloids Surf A Physicochem Eng Asp 580:123701. https://doi.org/10.1016/j.colsurfa.2019.123701
34. Gul I, Sayed M, Saeed T, Rehman F, Naeem A, Gul S, Khan Q, Naz K, ur Rehman M (2024) Unveiling cutting-edge progress in the fundamentals of MXene: synthesis strategies, energy and bio-environmental applications. Coord Chem Rev 511:215870. https://doi.org/10.1016/j.ccr.2024.215870
35. Ahmad S, Aminzai MT, Sharif T, Sayed M, Khan S, Rehman F, Khan JA, Yabalak E (2025) Advanced oxidation pathways for chlorophenol degradation-UV/H2O2 and UV/O3 kinetics and mechanisms. J Mater Sci 60:1–35. https://doi.org/10.1007/s10853-025-11745-1
36. Karim AV, Boczkaj G, Shriwastav A (2024) Effective sonophotocatalytic degradation of tetracycline in water: optimization, kinetic modeling, and degradation pathways. Chem Eng Process Process Intensif 205:109979. https://doi.org/10.1016/j.cep.2024.109979
37. Han K, Dong G, Saeed I, Dong T, Xiao C (2024) Morphology and photocatalytic tetracycline degradation of g-C3N4 optimized by the coal gangue. Chin J Struct Chem 43(2):100208. https://doi.org/10.1016/j.cjsc.2023.100208
38. Koysuren HN, Yahya SA, Koysuren O (2025) Sonophotocatalytic antibiotic degradation efficiency of g-C3N4/TiFe2O4. J Inorg Organomet Polym Mater 25:1–21. https://doi.org/10.1007/s10904-025-04153-0
39. Wang B, Liu X, Dai S, Lu H (2020) α− Fe2O3 nanoparticles/porous g− C3N4 hybrids synthesized by calcinations of Fe-based MOF/melamine mixtures for boosting visible-light photocatalytic tetracycline degradation. ChemSelect 5(11):3303–3311. https://doi.org/10.1002/slct.201904388
40. Guo J, Li P, Yang Z (2019) A novel Z-scheme g-C3N4/LaCoO3 heterojunction with enhanced photocatalytic activity in degradation of tetracycline hydrochloride. Catal Commun 122:63–67. https://doi.org/10.1016/j.catcom.2019.01.022
41. Salavati H, Tavakkoli N, Hosseinpoor M (2012) Preparation and characterization of polyphosphotungstate/ZrO2 nanocomposite and their sonocatalytic and photocatalytic activity under UV light illumination. Ultrason Sonochem 19(3):546–553. https://doi.org/10.1016/j.ultsonch.2011.09.001
42. Khanbeiki O, Ghasemi S, Emadi H (2024) Preparation of NiFe layered double hydroxide/graphitic carbon nitride nanocomposite for enhanced sonocatalytic deterioration of tetracycline hydrochloride. Diamond Relat Mater 143:110852. https://doi.org/10.1016/j.diamond.2024.110852